Electrochemically-Driven Abnormal Grain Growth of Ionic Ceramics

K. S. N. Vikrant,[†], Wolfgang Rheinheimer,[†], Hadas Sternlicht, [¶], Michael Bäurer,[‡], Michael J. Hoffmann,[‡], and R. Edwin García[†,*]

May 17, 2019

†: School of Materials Engineering,
Purdue University, West Lafayette, IN 47907, USA.
¶: School of Engineering,
Brown University, Providence, RI 02912, USA.
‡: Department of Ceramics in Mechanical Engineering,
Karlsruhe Institute of Technology, Karlsruhe, 76131,Germany.
∗: Contact author. phone:(765) 463-7801; email: redwing@purdue.edu

Abstract

A combined theoretical and experimental analysis was performed to understand the effects of extrinsic ionic species and point defects on the microstructural evolution of ionic polycrystalline ceramics. The model naturally incorporates the effects of drag as imposed by the interfacially accumulated charged defects for Fe doped $SrTiO_3$. Two moving grain boundary types, highly mobile and immobile interfaces are identified, resulting in abnormal grain growth. The fast moving grain boundaries leave a residual charge network in the interior of the grains, which are conformed of bands of $[Fe'_{Ti}]$, electrostatically attracts oxygen vacancies, thus enhancing the local ionic conductivity. Three grain size populations are statistically identified: (a) the *normal* grain population, as one would expect would happen in classical systems; (b) the *abnormal*, large grain population, which corresponds to those grains whose spatial extent is statistically greater than the average; and (c) an *electrochemically persistent* small grain size population that is stabilized by the grain boundary electrical energy. The developed theory sets the stage to assess the effects of externally applied fields such as temperature, electromagnetic fields, stresses and chemical stimuli to control the abnormal grain growth for developing a textured, oriented microstructures desirable for a wide range of applications.

Keywords: charged interfaces; moving interfaces; electrochemical drag; abnormal grain growth.

1 Introduction

Perovskite-type materials have been the subject of extensive studies due to their potential applications in energy production, storage, and usage [1]. The versatile properties of pervoskites such as transport, magnetic, ferroelectric, optoelectronic and thermoelectric properties are tunable using thermal and chemical stimuli by changing the underlying defect chemistry [2–6]. Additionally, modifications of the microstructure and interfacial characteristics further optimizes the macroscopic properties of these materials. Therefore, understanding the microstructural evolution of the pervoskites is a necessary step to tailor microstructures for various applications such as sensors, solid oxide fuel cells, actuators, capacitors, thermoelectric generator, magnets and memories.

Few experimental studies have investigated the effect of structural and electrochemical characteristics of grain boundaries on microstructural evolution in ionic solids. Specifically, in the case of strontium titanate, microstructures displaying abnormal grain growth with a bimodal grain size distribution have been observed. Here, at 1350°C (see Figure 1 (a)) the microstructure displays a traditional, large grain size, unimodal distribution. The increase in temperature favors the appearance of small grains in the microstructure. At 1425°C (see Figure 1 (d)), the grain size microstructure becomes abnormal. In this context, abnormal grain growth is a coarsening phenomenon where a small population of large grains grow appreciably faster than the average, and the grain size distribution is bimodal [7]. Numerous cases of abnormal grain growth are observed in metallic and ceramic systems. For example, it has been well documented that Al-Mn [8], Fe-Si [9, 10], Al-Cu [11], and FCC alloys [12], displayed abnormal grain growth due to high mobile, special CSL grain boundaries which are less prone to solute drag forces. Experimental investigations on Silver [13], 316L steels [14] and $BaTiO_3$ [2, 3] indicate that faceted grain boundaries are responsible for abnormal grain growth. Especially in $BaTiO_3$, high mobile faceted grain boundaries coexist with low mobile

rough grain boundaries leading to bimodal microstructures [2, 3]. The high anisotropy in solid/liquid interfacial energy in Al_2O_3, WC-Co, SiC shows a microstructure of abnormal grains with glassy films in between grains. Another way to obtain abnormal grain growth microstructures is by adding solute atoms to grain matrix. For example, abnormal grain growth is encouraged in Nb-doped strontium titanate to enhance thermoelectric properties [4], in (Nb, Ba)-doped TiO_2 to improve dielectric properties [5], and in halides-doped $CH_3NH_3PbI_{3-x}Cl_x$ to increase transport properties [6].

Monte Carlo approaches have been developed to understand abnormal grain growth, including the work of Rollet and coauthors [15], who used anisotropic grain boundary energies and mobilities. Lee and coworkers employed a percolating subset of grain boundaries of low interfacial energy to simulate the appearance of large grains in the Fe-Si system [16]. Recently, Holm and coauthors used pinning particles on grain boundaries to generate abnormal sized grains in 3D microstructures [17].

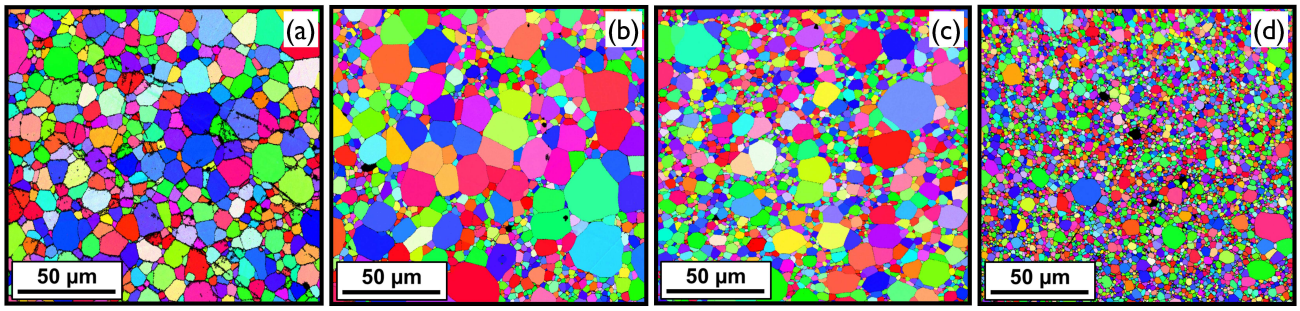

Figure 1: Microstructures of $SrTiO_3$ after ten hours at different temperatures: 1350°C (inset (a)), 1390°C (inset (b)), 1400°C (inset (c)), and 1425°C (inset (d)). With increasing temperature, fraction of small grains increases, which is mainly associated to electrochemical drag on grain boundaries [18].

Prior studies in substitutional or intrinsic ionic solids showed that the structural inhomogeneities of grain boundaries accumulates or depletes charge in its surroundings [19, 20]. Several authors described the accumulation/depletion zones via space-charge layers for thermodynamically stable grain boundaries. Descriptions include Guoy-Chapman in the dilute

limit of infinitesimally thin grain boundaries [20–24], and Mott-Schottky corrections to incorporate the grain boundary core effect for immobile dopants/substituents [25–29]. Mebane and DeSouza were the first to aim to describe the high substitution limit, while including the effects of a gradient energy penalty, [30]. Recently, Vikrant, Chueh, and García developed a comprehensive space-charge treatment that captures the electrochemomechanical equilibrium of a grain boundary with the abutting crystalline grains [31]. Most recently, the developed theory was extended to capture the effect of misorientation on the interfacial electrochemical and structural equilibrium and the resultant interfacial phase transitions, as well as its impact on the ionic transport properties [32].

In this paper, a thermodynamically consistent variational theory is proposed to model the microstructural kinetics evolution of polycrystalline ionic ceramics. Specifically, the developed model provides a rational basis to understand the drag effects of solute, point defects on the grain boundaries and its effect on the abnormal grain growth. The theory is demonstrated on Fe doped $SrTiO_3$ and validated against experimentally observed microstructures, also reported herein.

2 Theoretical Framework

Define the Helmholtz free energy per unit volume, f, for a polycrystal as a function of the degree of crystallinity, η, and N chemical species, $\{[V_i^{Z_i}]\} = \{[V_1^{Z_1}], \ldots, [V_N^{Z_N}]\}$, as classically defined [33]. Here, η is a coarse-grained measure of structural disorder, so that $\eta = 1$ defines a perfectly crystalline lattice and $\eta = 0$ defines a structurally disordered state. In addition, the i-th chemical component displays a valence, Z_i, which in turn contributes electrostatic energy from increasing the electrostatic charge, $\rho\phi$, and from increasing its dipolar moment density, $\frac{1}{2}\vec{D} \cdot \vec{E}$, to the system through the extended free energy, $f_\circ$, in agreement with

Hart [34], García *et al.* [35], and recent work [31]:

$$f_\circ(\eta, \{[V_i^{Z_i}]\}, \rho, \vec{D}, T) = f(\eta, \{[V_i^{Z_i}]\}, T) + \rho\phi + \frac{1}{2}\vec{D} \cdot \vec{E} \tag{1}$$

Equation 1 is a function of the coarse-grained charge density, ρ, the density of polarization, $\vec{D}$, and the position-dependent electric field, $\vec{E}$. In general, the resultant electric field is induced either by the surrounding electrostatic charge, or through the application of an external voltage difference. The spatial distribution of electrostatic charge raises the free energy of the system, $f_\circ$, when ρ has the same sign as the voltage, ϕ, at that same location. Thus, the second term on the right hand side of Equation 1 favors the intermixing of spatial charge of opposite polarity, or promotes the local depletion of charge from those regions whose voltage has the same polarity as the charged species that attempts to locally occupy it.

The electrochemical free energy density, f_{ec}, of the system is defined through the Legendre transformation $f_{ec}(\eta, \{[V_i^{Z_i}]\}, \vec{E}, T) = f_\circ(\eta, \{[V_i^{Z_i}]\}, \vec{D}, T) - \vec{D} \cdot \vec{E}$ [36, 37], which specifies that when the material is electrostatically polarized, there is a decrease in free energy density, in agreement with several authors [31, 35, 38, 39]. In addition, for a constant magnetic field, the position-dependent electric field, $\vec{E}$, is a solution of Faraday's Law, $\nabla \times \vec{E} = \vec{0}$, thus, the voltage distribution, ϕ, and the electric field are related through the relation, $\vec{E} = -\nabla\phi$. Finally, in the absence of ferroelectricity, the total polarization and the electric field are related through the constitutive equation, $\vec{D} = \epsilon\vec{E} = -\epsilon\nabla\phi$.

Following the work of Kobayashi, Warren, and Carter [40], each single crystal grain in a two-dimensional polycrystalline ionic solid is distinguished by an order parameter, θ, which measures the local orientation of a crystal with respect to a fixed laboratory reference frame. The two abutting crystals develop a grain boundary which add an interfacial grain boundary energy penalty as a function of the local misorientation, $|\nabla\theta|$, and the local crystalinity, η,

both of which are coupled through the monotonically increasing function $g(\eta) = \eta^p$, $p = 2 > 1$. $s_1 g(\eta)|\nabla\theta|$ corresponds to a monotonic increase in the grain boundary energy, which reduces to the classical Read-Shockley interface model in the limit of a sharp interface [40]. An additional higher order term of $\frac{s_2}{2} g(\eta)|\nabla\theta|^2$ is used for the grain boundary motion due to curvature. Here, s_1 and s_2 represents a structural coupling parameter as proposed by Warren and coworkers [41]. The sum of all the contributions to the total free energy functional is given by:

$$\begin{aligned} F[\eta, \theta, \{[V_i^{Z_i}]\}, \rho, \phi; T] &= \int_\Omega \Big[f(\eta, \{[V_i^{Z_i}]\}, T) \\ &\quad + \tfrac{\alpha^2}{2} (\nabla\eta)^2 + s_1 g(\eta)|\nabla\theta| + \tfrac{s_2}{2} g(\eta)|\nabla\theta|^2 \\ &\quad + \rho\phi - \tfrac{\epsilon}{2} (\nabla\phi)^2 \Big] d\Omega \end{aligned} \tag{2}$$

In agreement with recent work, [31, 32], Equation 2 defines the equilibrium of an ionic ceramic with electrostatically active grain boundaries as a function of the controlling variables, $\{[V_i^{Z_i}]\}, \eta, \theta, \rho, \phi$. For ease in the description, volumetric, conserved or non-conserved, phase transformations such as chemical phase separation are not included; however, they can be easily incorporated, *e.g.*, see [31, 42–45]. The local charge density imposes an additional physical constraint to the spatial distribution of the i-th species through the expression: $\rho = \sum_{i=1}^{N} e Z_i [V_i^{Z_i}]$ [31, 32, 35, 38, 39].

The effect of solute and chemical defect interactions is incorporated by extending Tang's work for metallic, electrically neutral grain boundary complexions, [44], and incorporating

the effect of point defects by using standard defect equilibria concepts [37]:

$$\begin{aligned} f(\eta, \{[V_i^{Z_i}]\}, T) &= \frac{1}{\nu}\Big(\sum_{i=1}^{N}(f_i(\eta,T)[V_i^{Z_i}] + k_bT[V_i^{Z_i}]\ln[V_i^{Z_i}]) \\ &\quad + k_bT(1-\sum_{i=1}^{N}[V_i^{Z_i}])\ln[1-\sum_{i=1}^{N}[V_i^{Z_i}]] \\ &\quad + \sum_{j=1,i\neq j}^{N}\Omega_{ij}[V_i^{Z_i}][V_j^{Z_j}]\Big) + \\ &\quad \frac{\alpha^2}{2}\eta^2(1-\eta)^2 + \Delta H\frac{\Delta T}{T_m}p(\eta) \end{aligned} \tag{3}$$

where the free energy contribution from the i-th component is $f_i(\eta,T) = f_i^X(T)p(\eta) + f_i^S(T)(1-p(\eta))$. Equation 3 reduces to the work reported by Tang *et al.*, in the limit of a binary, electrically neutral system [44].

For small deviations away from equilibrium, the variational derivatives associated to Equation **??** constitute the driving forces for microstructural evolution. The resultant kinetic equations are:

$$\begin{aligned} \frac{\partial\theta}{\partial t} &= -M_\theta[g(\eta)(-s_1\nabla\cdot\frac{\nabla\theta}{|\nabla\theta|} - s_2\nabla^2\theta)] \\ \frac{\partial\eta}{\partial t} &= -M_\eta[\frac{\partial f}{\partial\eta} - \alpha^2\nabla^2\eta + \frac{\partial g}{\partial\eta}(s_1|\nabla\theta| + \frac{s_2}{2}|\nabla\theta|^2)] \\ \frac{\partial[V_i^{Z_i}]}{\partial t} &= \nabla\cdot M_{[V_i^{Z_i}]}\nabla[\frac{\partial f}{\partial[V_i^{Z_i}]} + Z_ie\phi] \\ \frac{\delta F}{\delta\phi} &= \nabla\cdot\epsilon\nabla\phi + \rho = 0 \end{aligned} \tag{4}$$

Specifically, the structural order defines a locally non-conserved order parameter, follows Allen-Cahn kinetics [33, 40]. Similarly, the crystallographic orientation of every grain is a non-conserved quantity, in agreement with Kobayashi and coworkers [40], and later Tang *et al.* [33]. The first and second rows of Equation 4 represent the dynamics of microstructural evolution via grain boundary migration and grain rotation. The third row of Equation 4 corresponds to the mass conservation equation of the i-th component in agreement with several authors [35, 38]. Finally, the fourth row of Equation **??** corresponds to Coulomb's equation, in agreement with several authors [31, 32, 35, 38, 39].

3 Numerical Implementation

Simulated polycrystalline two-dimensional microstructure were initialized as a voronoi tessellation, where the orientation of each grain was assigned from a random crystallographic orientation distribution, as shown in Figure 2. The initial $[V_O^{\cdot\cdot}]$ and $[Fe_{Ti}^{\prime}]$ were set to its experimental equilibrium values based on Fe dopants concentration in $SrTiO_3$ [46]. Fe doped $SrTiO_3$ properties are summarized in Table 1. Electrically, the right edge of the simulation domain was grounded and a no-flux boundary condition was set on the other edges. A no-flux boundary condition was set on all the edges for solute, point defect concentrations, structural and orientation order parameters. Equation set 4 and Coloumb's equation, were solved across a 1μm $\times$ 1μm simulation domain, and discretized into a 1000$\times$1000 finite volume mesh.

Simulations were carried out on a 2.6 GHz, 16 core, Ubuntu 16.04 workstation with 128 GB of RAM. Equation set 4 were implemented in FiPy [47]. The relative tolerance for convergence was set to 1×10^{-8}. Each one-dimensional calculation took on the order of one hour of wall time to complete. 20 hours of two-dimensional grain coarsening simulations took on the order of 15 days of wall time to complete. The grain coarsening statistics were obtained using a watershed algorithm in ImageJ, where the structural threshold, η_{th}, was less than 0.98 to identify different grain boundaries. The bin width is calculated using Freedman-Diaconis rule [48]. The obtained grain size distribution was fitted as a sum of weighted lognormal distribution functions, $\mathrm{PDF}(\hat{r}) = \sum_{i=1}^{n} w_i \mathcal{N}(\hat{r}, m_i, d_i)$, where $\hat{r} = \frac{R}{\langle R \rangle}$, the normalized grain size, w_i, the proportionality coefficient, m_i is the mean grain size, d_i is the standard deviation, and $\mathcal{N}(\hat{r}, m_i, d_i) = d_i\sqrt{2\pi}\hat{r}\exp(-\frac{1}{2}(\frac{(\ln(\hat{r})-m_i)}{d_i})^2)$ is the lognormal distribution of the i-th population.

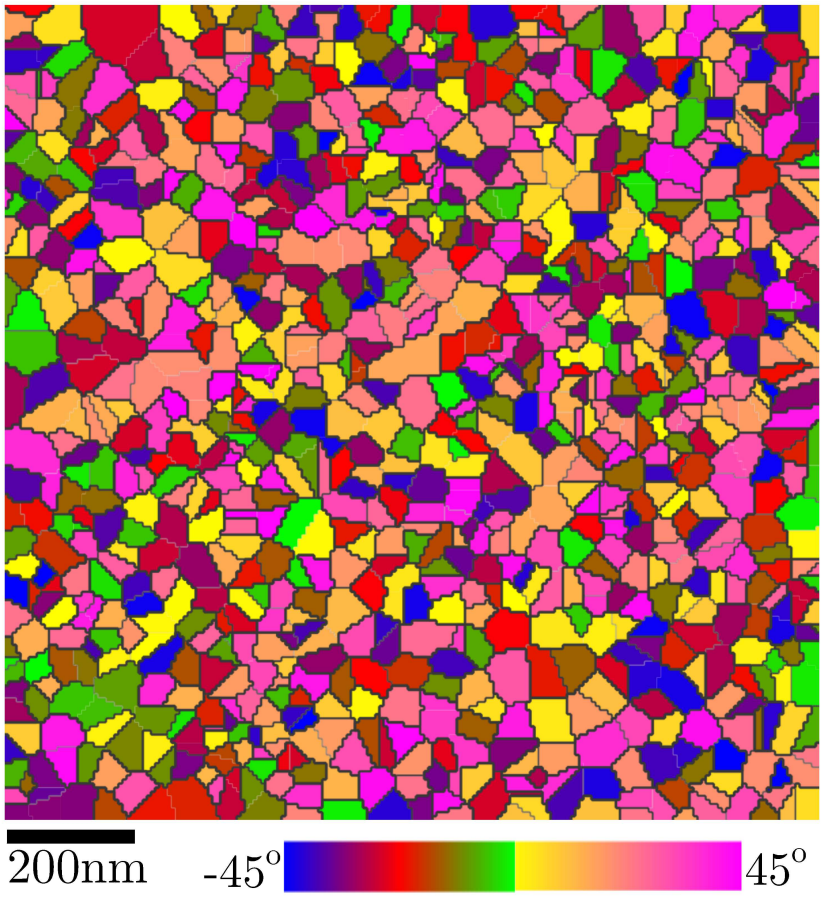

Figure 2: Grain growth simulation setup. Grains with random crystallographic orientations were generated using a voronoi tessellation. The right edge of the simulation domain was set to be electrically grounded and a no-flux boundary condition was set on the other edges. A no-flux boundary condition was set on all the edges for solute, point defect concentrations, structural and orientation order parameters.

4 Experimental Procedure

High purity stoichiometric strontium titanate powder was synthetized by the mixed oxide/-carbonate method ($SrCO_3$ and TiO_2, purity of 99.95% and 99.995%, Sigma Aldrich Chemie GmbH, Taufkirchen,Germany). Fe_2O_3 was used (purity of >99%, Merck, Darmstadt, Germany) as acceptor dopant. Here, Fe occupies the B-site of the perovskite of 0.2at%, 2at%

Table 1: Summary of physical parameters used in grain growth calculations for $SrTiO_3$.

Parameter	Symbol	Value	Units	Ref.
Oxygen vacancies ionic valence	Z_O	2	–	–
Fe defects ionic valence	Z_{Fe}	-1	–	–
Segregation energy of oxygen vacancies to grain boundary	$f^{GB}_{V_O^{\cdot\cdot}} - f^{X}_{V_O^{\cdot\cdot}}$	-0.8	eV	[46]
Segregation energy of Fe defects to grain boundary	$f^{GB}_{Fe'_{Ti}} - f^{X}_{Fe'_{Ti}}$	0.0	eV	[46]
Atomic volume of Strontium Titanate	ν	5.96×10^{-29}	m^3/atom	–
Latent heat of fusion	ΔH	1.9×10^9	J/m^3	–
Melting temperature	T_m	2353	K	–
Order-disorder interfacial energy	γ	0.6	J/m^2	[18]
Order-disorder interfacial thickness	δ	1	nm	–
Grain boundary energy penalty coefficient	$\alpha = \sqrt{6\gamma\delta}$	6×10^{-5}	$(J/m)^{1/2}$	[45]
Barrier height scaling parameter	$a = \sqrt{6\frac{\gamma}{\delta}}$	6×10^4	$\sqrt{J/m^3}$	[45]
Structural coupling parameter	$s_1 = \frac{2a\alpha}{\Delta\theta_{max}}$	9.2	J/m^2	[41]
Curvature coupling parameter	s_2	0.008	J/m	[41]
Diffusion coefficient of oxygen vacancies	D_O	1.35×10^{-9}	m^2/s	[46]
Diffusion coefficient of Fe defects	D_{Fe}	1.3×10^{-11}	m^2/s	[46]
Allen-Cahn mobility for crystalline transformation	M_η	6×10^{-8}	m/Js^3	–
Allen-Cahn mobility for orientation transformation	M_θ	6×10^{-7}	m/Js^3	–
Relative dielectric permittivity of $SrTiO_3$	ϵ_r	56	–	[46]

or 5at% Ti of strontium titanate. After attrition milling, calcination and ball milling the powder particle size was below 1μm (median of 0.5μm). Green bodies were pressed cold-isostatically with 400 MPa. Sintering and grain growth experiments were done in a tube furnace (HTK 16K, Carbolite Gero GmbH & Co. KG, Neuhausen, Germany) in oxygen between 1300°C and 1460°C. Samples were cut, polished and thermal etching was used to ease SEM observation of the microstructures. Further details on the powder synthesis and sample preparation are published elsewhere [46, 49]. Microstructures were observed by SEM (Leica Leo Stereoscan 440 and FEI Nova NanoSEM 450). Grain size distributions were obtained from at least 300 grains. For TEM characterization, samples were water-quenched to sustain the high-temperature state of the interface. Cooling to below 100 °C was estimated to occur within 3s [50]. TEM samples were prepared using the conventional method, *i.e.*, slicing, mechanical thinning, dimpling, and ion milling with Ar. The samples were characterized using FEI Titan Cubed Themis G2 60-300 operated at 300KV.

5 Results and Discussion

The grain coarsening experimental results of $SrTiO_3$ at 1350°C are summarized in Figure 3. Unimodal microstructures were found for undoped samples for all heating times (see Figure 3 (a), (b)(c)). However, an increasing fraction of very small grains with a size of roughly 100nm is evident in the microstructures with increasing Fe concentration. For Fe=0.2% (see Figure 3 (a),(d)), the small grains population decreases with time, as the large grains grow and consume the small grains, as one would classically expect. An increase in Fe dopant concentration to 2% results in the formation of a larger population of very small grains around large grains exhibiting a bimodal grain size *i.e.*, abnormal grain growth (see Figure 3 (b)). These small grains are consumed over time by the large grain size population (see

Figure 3 (d)). For Fe=5% (see Figure 3 (c),(f)), grain growth is severely stunted, and grains are small and pinned. Overall, an increase in Fe dopant concentration has a similar effect on the microstructure evolution as an increasing temperature on $SrTiO_3$ as shown in Figure 1.

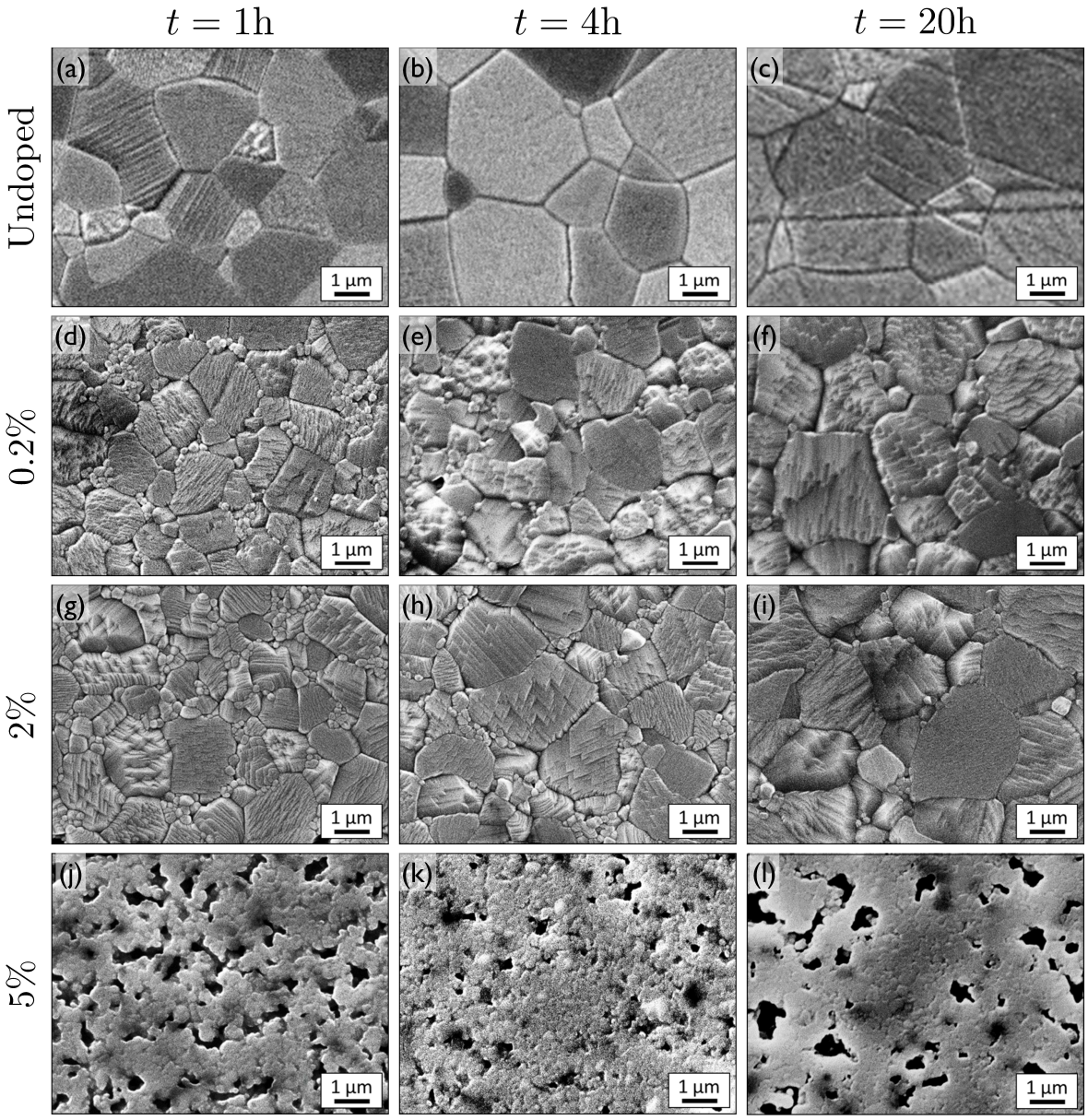

Figure 3: Microstructure of $SrTiO_3$ at 1350°C for different heating times: 1h (left column), 4h (middle column) and 20h (right column). Every row defines a different amount of Fe dopant concentrations: undoped (first row), 0.2% (second row), 2% (third row) and 5%(last row).

The distribution of Fe at the interfaces was measured by STEM-EDS for 2% Fe concentration after 4.5h at 1350°C as shown in Figure 4. Notice the difference in scale. As evident in the higher resolution images in Figure 4 (b) and (c), no separate phase was detected along the grain boundaries or in triple pockets. Fe was found to segregate to the grain boundaries as evident in Figure 4 (d)-(f). The segregation does not occur only to the gain boundary core, but forms a diffuse layer the interface with a thickness in the order of 5-20nm. As shown in Figure 4(a), not all grain boundaries have the same amount of Fe segregation and its special extend. In addition, the Fe concentration of Fe in the bulk of the grains varies as some grains hardly have any Fe in the core, while others have considerable concentrations. Overall, the Fe concentration in the bulk of the grains is somewhat patchy.

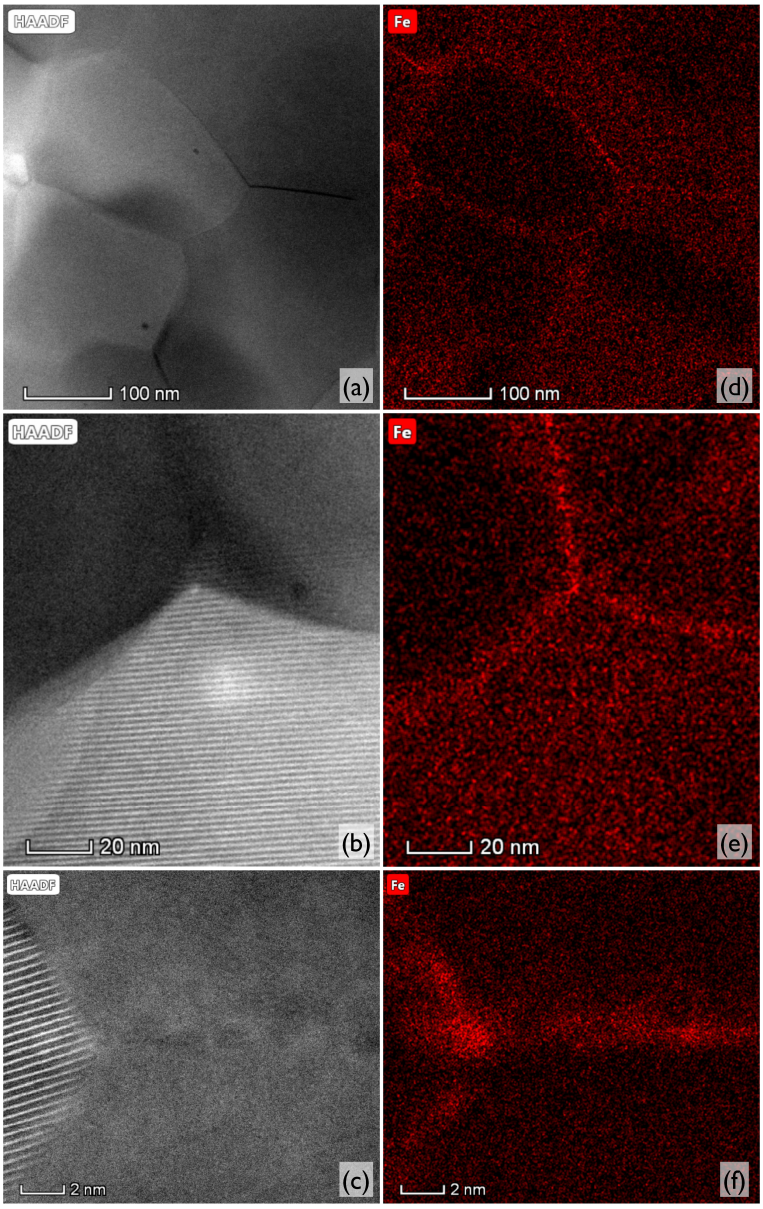

Figure 4: HAADF images (a-c) and concentration mapping of Fe as obtained by STEM-EDS for the same regions (d-f) for 2% Fe after 4.5h at 1350°C with water-quenching. Notice the difference in the scale.

Figure 5 shows the grain coarsening of polycrystalline $SrTiO_3$ at 1350°C for Fe=2%. Results demonstrate the clear appearance of three charged populations: (i) small angle misorientation grain boundaries, which are thin, structurally ordered; (ii) large angle misorientation grain boundaries, which are thick, structurally disordered interfaces; and (iii) a

very small population of negatively charged grains. Structurally thick grain boundaries favor oxygen vacancies, which increases the grain boundary core charge density and a wide negative space charge in the vicinity of the grain boundary core (see Figure 5 (d),(e),(f)). The large positive core charge density of structurally thick grain boundaries and triple junctions, as well as the charge and solute asymmetry that develops in the vicinity of curved grain boundaries leads to an increase of the local electrostatic potential which, in turn, extends across long microstructural distances, (see Figure 5 (g),(h),(i)). In contrast, the negative charge regions adjacent to a small angle misorientation is negligible. Here, first order grain boundary structural and chemical transitions are absent, but grain boundaries continuously transition from ordered to disordered as a function of misorientation. Further, triple junctions are structurally more disordered than large angle grain boundaries and display a high positive core charge density, becoming naturally highly energetic, but kinetically pinned. In addition, the neighborhood of grain boundaries with negative radius of curvature have wide depleted negative space charge layers and large electrostatic potential gradients. Finally, grains whose diameter is comparable to the width of the space charge layer become fully negatively charged due to the depletion of $[V_O^{\cdot\cdot}]$ and $[Fe'_{Ti}]$. These grains are attempting to disappear because of the small radius of curvature, but its disappearance is delayed by the electrostatic repulsion of the facing charged interfaces.

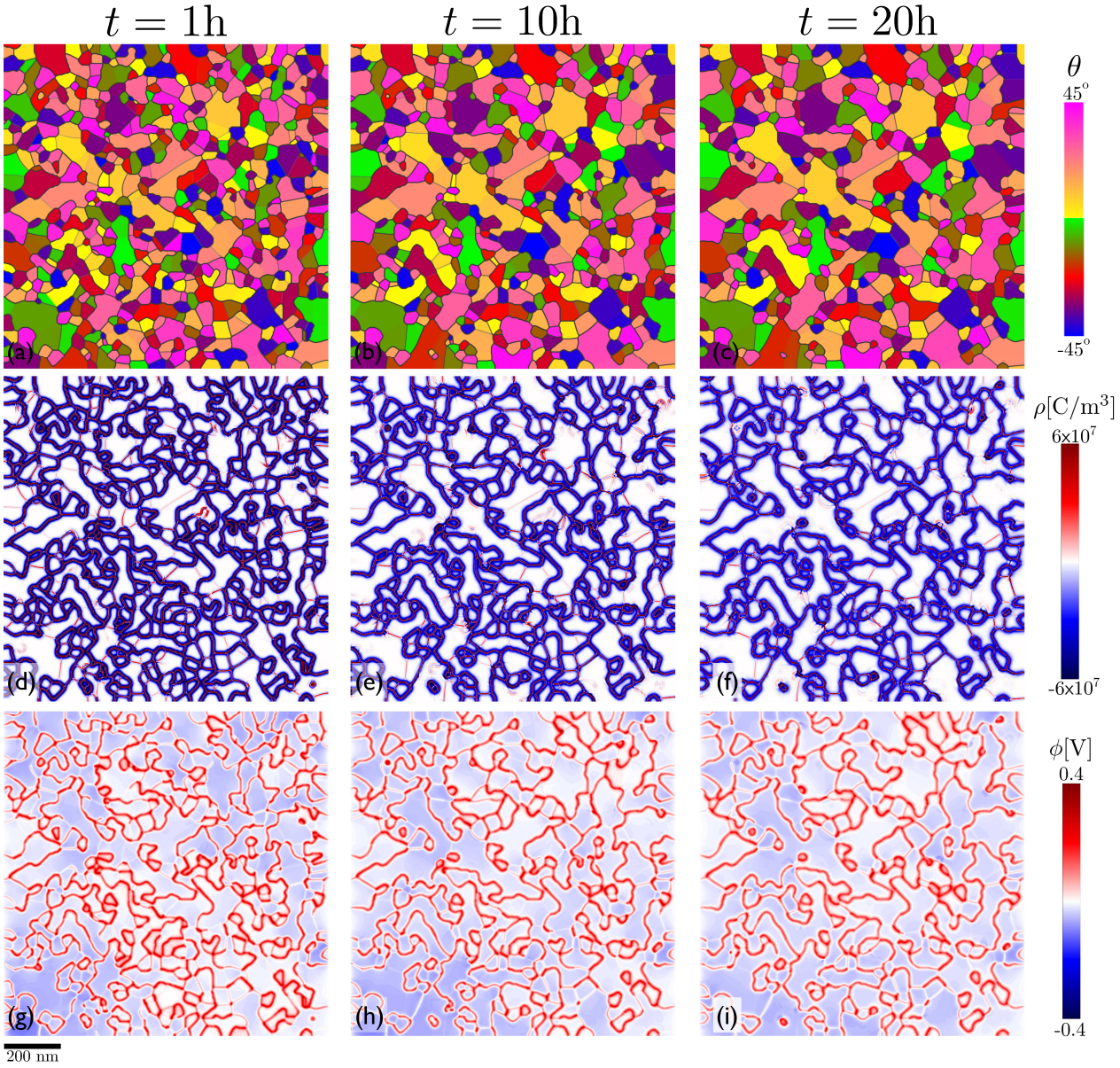

Figure 5: Grain growth of $SrTiO_3$ at 1350°C for Fe dopant concentrations of 2% at selected times: 1h (left column), 10h (middle column), and 20h (right column). The top row shows the microstructure evolution represented by an orientation field. The middle row shows the corresponding charge density distribution. The bottom row shows the corresponding local electrostatic potential.

During the grain growth process, small angle misorientations experience low electrochemical drag force because of small grain boundary core charge density and negligible space charge

layers. In contrast, enhanced grain boundary core segregation followed by wide depletion space charge layers in large angle misorientations and triple junctions slow the grain growth due to high electrochemical drag force. Calculations demonstrate that in Fe-doped $SrTiO_3$ polycrystals for ion conductor applications, thick, large angle misorientations will favor fast ionic conduction paths along the interfaces. In contrast, small angle grain boundaries will favor fast ionic conduction paths across the interfaces due to the narrow depletion zone of oxygen vacancies in the immediate neighborhood of interface. The grains whose diameter is comparable to the width of the space charge layer have low ionic conductivity due to depletion of $[V_O^{\cdot\cdot}]$ inside the grain.

When the grain boundaries and triple junctions overcome the electrochemical energy barrier imposed by a charged grain boundary microstructure, they will move fast and will leave a space charge in the grain matrix , persisting long after the grain has disappeared. This is in agreement with the solute separation from grain boundaries in metallic systems [51, 52]. As the grain growth progresses, the oxygen vacancies in the residual space charge slowly diffuses to the interior grain region and bands of negatively charged Fe are left behind. The inhomogeneous, excess negatively charged $[Fe'_{Ti}]$ in the interior of grains electrostatically attracts the positively charged $[V_O^{\cdot\cdot}]$ adjacent to it, locally stabilizing it. Here, the residual charge network in the grain interior is p-n-p type, opposite to the grain boundary space charge network of n-p-n type. The residual charge network has a local negative electrostatic potential contrary to a positive electrostatic potential of grain boundaries. The residual charge network in the interior grains enhance the local ionic conductivity due to excess oxygen vacancies, adding internal charge conduction shortcuts, which provide a new and previously unexplored degree of freedom to tailor material properties.

The effect of Fe doping on the grain growth of $SrTiO_3$ at 1350°C is shown in Figure 6. Results demonstrate that as the macroscopic concentration of Fe increases, the disorder of

the interface increases and favors thick grain boundaries (see Figure 6 (a), (b), (c)). Further, the grain boundary core charge density increases as the average amount of Fe dopant increases (see Figure 6 (d), (e), (f)), even though the width of negative space charge region in the vicinity of the grain boundaries shrink. For Fe=0.2%, the large grains are surrounded by a small population of grains smaller than the average size grains. For Fe=2% concentration, the fraction of small grains increases due to an increase in electrochemical drag force. As the dopant concentration increases, *e.g.*, Fe=5%, the grain boundary motion is further impeded by the grain boundary drag force as a result of the $[Fe'_{Ti}]$ accumulated at the interface. Further, the increase in average concentration of Fe completely suppresses grain rotation, particularly for small grains. A direct comparison of simulated and experimental microstructures shows a great qualitative agreement. In addition, because grain growth is completely suppressed, the extent of the residual charge network decreases with average concentration of Fe. However, a large fraction bands of Fe with its associated oxygen vacancies are left inside the grains of 5% Fe doped samples.

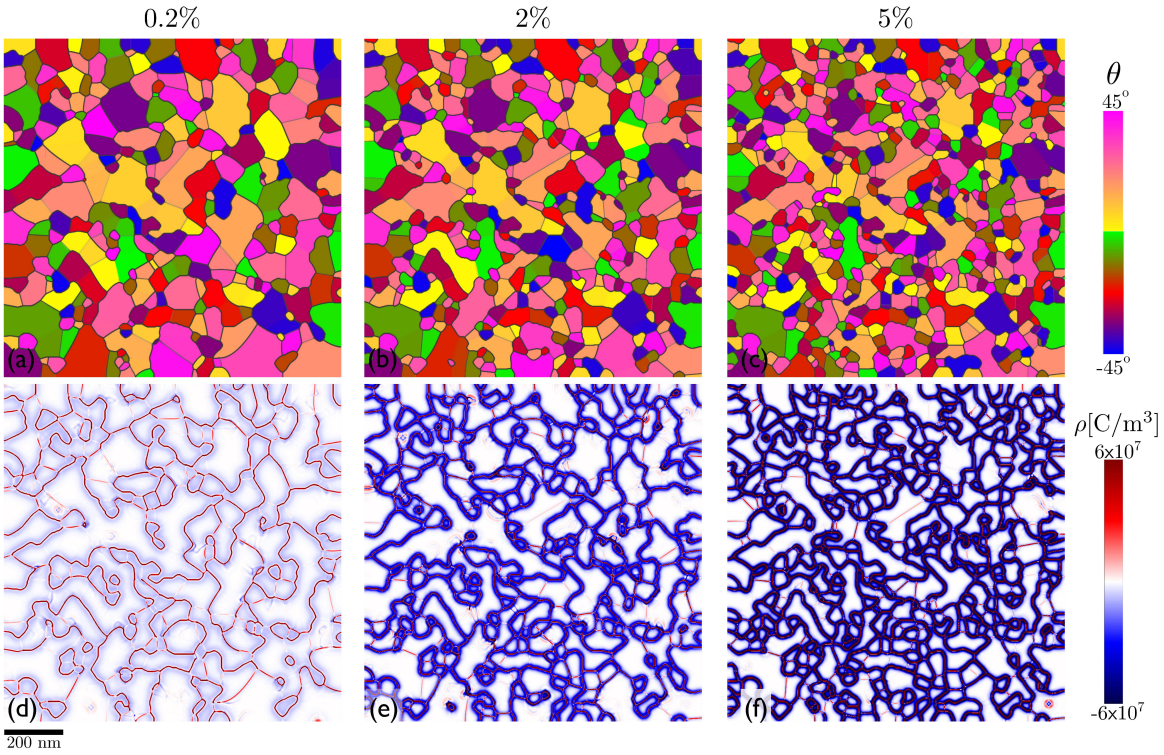

Figure 6: Grain growth of $SrTiO_3$ at 1350°C at t = 20h for Fe dopant concentrations: 0.2% (left column), 2% (middle column), and 5% (right column). The top row shows the microstructure evolution represented by an orientation field. The bottom row shows the corresponding charge density distribution.

Results demonstrate that the two types of grain boundaries induce two visually apparent grain size populations, that define the abnormal grain growth in Fe-dropped $SrTiO_3$. Figure 6 demonstrates that the collective grain interactions define two interlocked populations: a large grain size spatially continuous population decorated with clusters of small grains. The addition of Fe further pins grain boundaries increasing the subpopulation of smaller grains. Statistically, Figure 7 (a) demonstrates that there are in fact two populations, namely: (a) the *normal* grain population, as one would expect would happen in classical systems [53]; (b) the *abnormal*, large grain population, which corresponds to those few grains whose extent statistically stands out from the average.

A comparison against Figure 7 (b) and (c) shows that as Fe is added to the $SrTiO_3$

polycrystal, the average grain size decreases, as a result of the drag-force imposed on the interfaces. Addition of iron favors third population of a smaller grain size than the average, but statistically significant *electrochemically persistent* grain size population that is stabilized by the grain boundary electrical energy. Further, the number of abnormally growing grains is greatly depressed to a statistically favored few, while the electrochemically persistent population becomes indistinguishable from the normal population.

Additionally, experimental statistics (see Figure 7 (d) and (e)) are qualitatively in agreement with the simulations. Here, large grain population is far away from the average grain size. The simulation results can further be improved by considering 3D polycrystalline microstructures and anisotropy of the interfaces. Notice that for 5% Fe, no grain size distribution could be obtained.

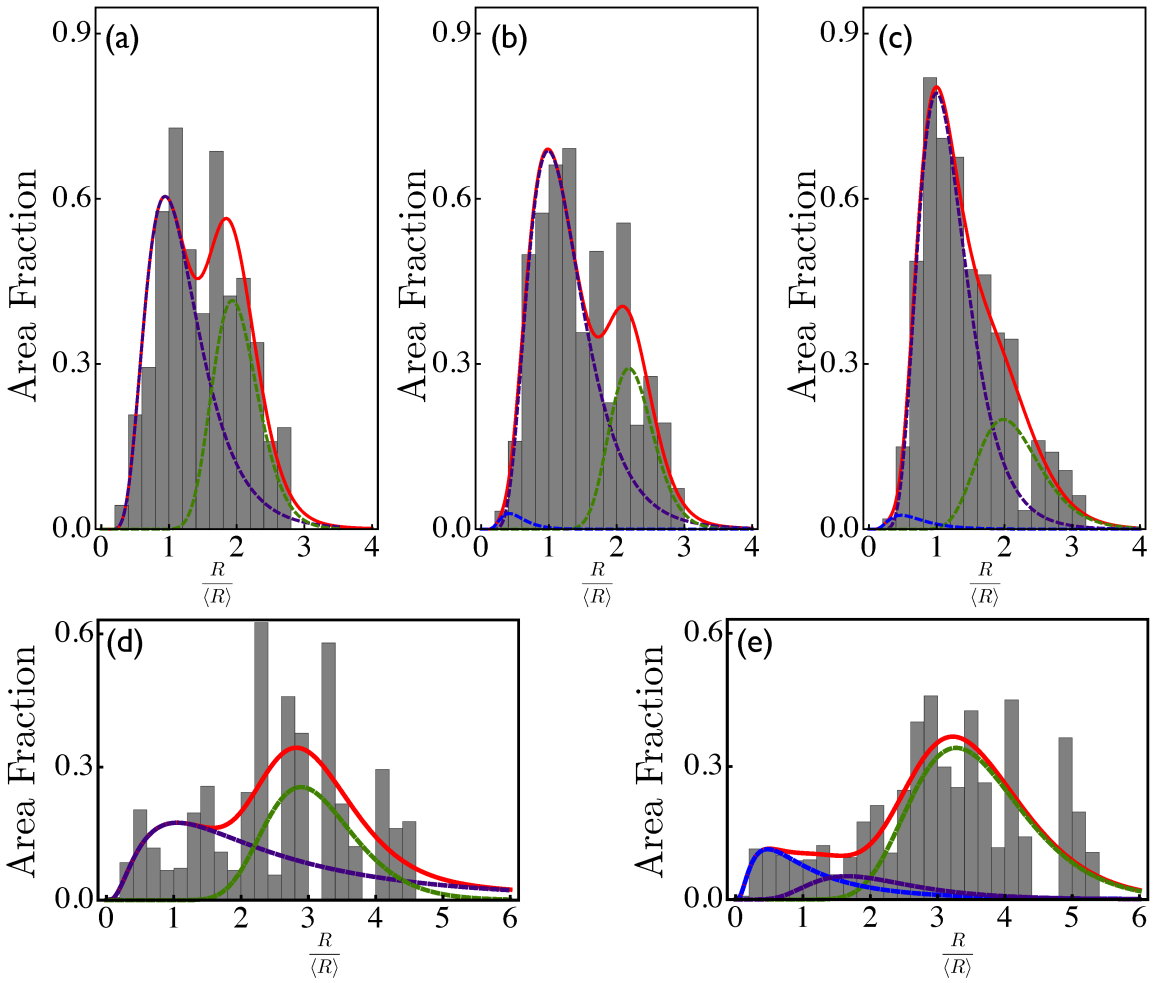

Figure 7: Simulated and experimental area distribution of $SrTiO_3$ at 1350°C for heating time of 20h. The top row shows the simulated area distribution for Fe dopant concentrations: 0.2% (inset (a)), 2%(inset (b)), 5% (inset (c)). The bottom row shows the experimental area distribution for Fe dopant concentrations: 0.2% (inset (d)), 2%(inset (e)). The total probability function (red line) is fitted as sum of log-normal distribution functions of large grain population (green dashed line), normal grain population (purple dashed line), and small grain population (blue dashed line). The fitted total distribution function for experiments: 0.2%, $\mathrm{PDF}(\hat{r}) = 0.84\mathcal{N}(\hat{r}, -0.267, 0.541) + 0.16\mathcal{N}(\hat{r}, 0.5715, 0.1963)$, 2%, $\mathrm{PDF}(\hat{r}) = 0.748\mathcal{N}(\hat{r}, -0.1591, 0.3561) + 0.094\mathcal{N}(\hat{r}, -0.8849, 0.3249) + 0.158\mathcal{N}(\hat{r}, 0.5305, 0.2732)$, and 5%, $\mathrm{PDF}(\hat{r}) = 0.051\mathcal{N}(\hat{r}, -0.9703, 0.596) + 0.882\mathcal{N}(\hat{r}, -0.105, 0.363) + 0.067\mathcal{N}(\hat{r}, 0.623, 0.2425)$. The fitted total distribution function for simulations: 0.2%, $\mathrm{PDF}(\hat{r}) = 0.57\mathcal{N}(\hat{r}, 0.789, 0.86) + 0.43\mathcal{N}(\hat{r}, 1.11, 0.226)$, and 2%, $\mathrm{PDF}(\hat{r}) = 0.729\mathcal{N}(\hat{r}, 1.25, 0.252) + 0.163\mathcal{N}(\hat{r}, -0.029, 0.847) + 0.108\mathcal{N}(\hat{r}, 0.705, 0.447)$.

6 Summary and Conclusions

A combined experimental and theoretical studies were conducted to explain abnormal grain growth in ionic solids with an emphasis on the structural and electrochemical character of the grain boundaries. Chemical segregation and space charge was demonstrated to contribute to the drag forces opposing grain boundary motion. Such driving forces are quantified to rationalize abnormal grain growth. The microstructural evolution study on Fe doped $SrTiO_3$ performed herein demonstrates that: a) small angle misorientation grain boundaries are thin, structurally ordered and experience low electrochemical drag force due to negligible space charge; b) large angle misorientations favor structurally thick, disordered interfaces with large grain boundary core segregation followed by a wide space charge layer. These interfaces experience a large electrochemical drag force; c) negatively charged grains, whose diameter is comparable to the width of the space charge layer; d) a residual charge network in the grain interior is stabilized due to the break away of the grain boundaries, resulting on bands of $[Fe'_{Ti}]$, which attract $[V^{\cdot\cdot}_{O}]$ adjacent to it. The accumulated oxygen vacancies in the interior of the grains increase the local ionic conductivity and provide previously identified shortcuts for charge transport.

The coexistence of high mobile drag-free grain boundaries with low mobile electrochemical forces opposing grain boundary motion result in a bimodal grain size distribution, *i.e.*, abnormal grain growth. Three grain size populations are statistically identified: (a) the *normal* grain population; (b) the *abnormal*, large grain population formed due to high mobile grain boundaries; and (c) an *electrochemically persistent* small grain size population that is stabilized due to electrostatic repulsion of the facing charged interfaces. An increase in the average concentration of Fe decreases the number of abnormally growing grains and the electrochemically persistent population becomes indistinguishable from the normal population.

7 Acknowledgments

The authors are very grateful for the support provided by US ONR N00014- 17-1-2087.

8 Conflict of interest

There are no conflicts of interest to declare.

References

[1] B. V. Lotsch and J. Maier. Relevance of solid electrolytes for lithium-based batteries: A realistic view. *J. Electro. Ceram.*, 2017.

[2] B. K. Lee, S. Y. Chung, and S. J. L. Kang. Grain boundary faceting and abnormal grain growth in $BaTiO_3$. *Acta Mater.*, 48:1575–1580, 2000.

[3] B. K. Lee, Y. I. Jung, S. J. L. Kang, and J. Nowotny. {111} twin formation and abnormal grain growth in (Ba,Sr)TiO_3. *J. Am. Ceram. Soc.*, 86:155–160, 2003.

[4] A. Tkach, J. Resende, K. V. Saravanan, M. E. Costa, P. Diaz-Chao, E. Guilmeau, O. Okhay, and P. M. Vilarinho. Abnormal grain growth as a method to enhance the thermoelectric performance of Nb-doped strontium titanate ceramics. *ACS Sustainable Chem. Eng.*, 6:15988–15994, 2018.

[5] C. J. Chen and J. M. Wu. The abnormal grain growth and dielectric properties of (Nb, Ba) doped TiO_2 ceramics. *J. Mat. Sci.*, 24:2871–2878, 1989.

[6] Q. Dong, Y. Yuan, Y. Shao, Y. Fang, Q. Wanga, and J. Huang. Abnormal crystal growth in $CH_3NH_3PbI_{3-x}Cl_x$ using a multi-cycle solution coating process. *Energy Environ. Sci.*, 8:2464–2470, 2015.

[7] S. J. L. Kang. *Sintering: Densification, Grain Growth and Microstructure*. Elsevier, 1st edition, 2005.

[8] P. R. Rios and G. Gottstein. Texture evolution during normal and abnormal grain growth in an Al-1wt% Mn alloy. *Acta Mater.*, 49:2511–2518, 2001.

[9] H. Homma and B. Hutchinson. Orientation dependence of secondary recrystallisation in silicon-iron. *Acta Mater.*, 51:3795–3805, 2003.

[10] N. Rajmohan and J. A. Szpunar. An analytical method for characterizing grain boundaries around growing goss grains during secondary recrystallization. *Scripta Mater.*, 44:2387–2392, 2001.

[11] J. Dennis, P. S. Bate, and F. J. Humphreys. Abnormal grain growth in metals. *Materials Science Forum*, 558–559:717–722, 2007.

[12] J. Bystrzycki, W. Przetakiewicz, and K. J. Kurzydlowski. Study of annealing twins and island grains in F.C.C. alloy. *Acta Metall. Mater.*, 41:2639–2649, 1993.

[13] J. B. Koo and D. Y. Yoon. The dependence of normal and abnormal grain growth in silver on annealing temperature and atmosphere. *Metall. Mater. Trans. A*, 32A:469–475, 2001.

[14] J. S. Choi and D. Y. Yoon. The temperature dependence of abnormal grain growth and grain boundary faceting in 316L stainless steel. *ISIJ International*, 41:478–483, 2001.

[15] A. D. Rollett, D. J. Srolovitz, and M. P. Anderson. Simulation and theory of abnormal grain growth: Anisotropic grain boundary energies and mobilities. *Acta metall.*, 37:1227–1240, 1989.

[16] D. K. Lee, K. J. Ko, B. J. Lee, and N. M. Hwang. Monte carlo simulations of abnormal grain growth by sub-boundary-enhanced solid-state wetting. *Scripta Materialia*, 58:683–686, 2008.

[17] E. A. Holm, T. D. Hoffmann, A. D. Rollett, and C. G. Roberts. Particle-assisted abnormal grain growth. *IOP Conf:Materials Science and Engineering*, 89:012005, 2015.

[18] W. Rheinheimer and M. J. Hoffmann. Grain growth in perovskites: What is the impact of boundary transitions? *Current Opinion in Solid State and Materials Science*, 20:286–298, 2016.

[19] J. Maier. Space-charge regions in solid 2-phase systems and their conduction contribution in conductance enhancement in the system ionic conductor-inert phase and application on AgCl-Al_2O_3 and AgCl-SiO_2. *Phys. Chem. Solid.*, 46:309–320, 1985.

[20] J. Maier. Ionic-conduction in space charge regions. *Prog. Solid. State. Chem.*, 23:171–263, 1995.

[21] J. Frenkel. *Kinetic Theory of Liquids*. Oxford University Press, New York, 36th edition, 1946.

[22] K. Lehovec. Space charge layer and distribution of lattice defects at the surface of ionic crystals. *J. Chem. Phys.*, 21:1123, 1953.

[23] J. D. Eshelby, C. W. A. Newey, P. L. Pratt, and A. B. Lidiard. Charged dislocations and the strength of ionic crystals. *Phil. Mag.*, 3:75–89, 1958.

[24] K. L. Kliewer and J. S. Koehler. Space charge in ionic crystals. I. General approach with application to NaCl. *Phys. Rev.*, 140:A1226–A1240, 1965.

[25] X. Guo, W. Sigle, and J. Maier. Blocking grain boundaries in yttria-doped and undoped ceria ceramics of high purity. *J. Am. Ceram. Soc.*, 86:77–87, 2003.

[26] S. Kim and J. Maier. On the conductivity mechanism of nanocrystalline ceria. *J. Elec. Soc.*, 149:J73–J83, 2002.

[27] J. Luo. Interfacial engineering of solid electrolytes. *J. Materiomics*, 1:22–32, 2015.

[28] N. F. Mott. Theory of crystal rectifiers. *Proc. Roy. Soc. (London) A.*, 171:27, 1939.

[29] W. Z. Schottky. Zur halbleitertheorie der sperrschicht- und spitzengleichrichter. *Physik*, 113:367, 1939.

[30] D. S. Mebane and R. A. De Souza. A generalised space charge theory for extended defects in oxygen-ion conducting electrolytes: From dilute to concentrated solid solutions. *Energy Environ. Sci.*, 8:2935, 2015.

[31] K. S. N. Vikrant, W. C. Chueh, and R. E. García. Charged interfaces: Electrochemical and mechanical effects. *Energy Environ. Sci.*, 11:1993–2000, 2018.

[32] K. S. N. Vikrant and R. E. García. Charged grain boundary transitions in ionic ceramics for energy applications. *npj Computational Materials*, 24:1–12, 2019.

[33] M. Tang, W. C. Carter, and R. M. Cannon. Diffuse interface model for structural transitions of grain boundaries. *Phys. Rev. B: Condens. Matter Mater. Phys.*, 73:024102, 2006.

[34] E. W. Hart. Thermodynamics of inhomogeneous systems. *Phys.Rev.*, 113:412–416, 1959.

[35] R. E. García, C. M. Bishop, and W. C. Carter. Thermodynamically consistent variational principles with applications to electrically and magnetically active systems. *Acta Mater.*, 52(1):11–21, 2004.

[36] J. W. Gibbs. On the equilibrium of heterogeneous substances. *Phys.Rev.*, 44:108–437, 1878.

[37] R. T. DeHoff. *Thermodynamics in Materials Science*. McGraw-Hill, New York, 2nd edition, 1993.

[38] C. M. Bishop, R. E. García, and W. C. Carter. Effect of charge separation on the stability of large wavelength fluctuations during spinodal decomposition. *Acta Mater.*, 51(6):1517–1524, 2003.

[39] J. E. Guyer, W. J. Boettinger, J. A. Warren, and G. B. McFadden. Phase field modeling of electrochemistry I: Equilibrium. *Phys. Rev. E.*, 69:021603, 2004.

[40] R. Kobayashi, J. A. Warren, and W. C. Carter. A continuum model of grain boundaries. *Physica D*, 140:141–150, 2000.

[41] J. A. Warren, R. Kobayashi, A. E. Lobkovsky, and W. C. Carter. Extending phase field models of solidification to polycrystalline materials. *Acta. Mater.*, 51:6035–6058, 2003.

[42] J. W. Cahn and J. E. Hilliard. Free energy of a nonuniform system. I. Interfacial free energy. *J. Chem. Phys.*, 28:258–267, 1958.

[43] J. W. Cahn. On spinodal decomposition. *Acta Metallurgica*, 9:795–801, 1961.

[44] M. Tang, W. C. Carter, and R. M. Cannon. Grain boundary transitions in binary alloys. *Phys. Rev. Lett.*, 97:075502, 2006.

[45] W. J. Boettinger, J. A. Warren, C. Beckermann, and A. Karma. Phase-field simulation of solidification. *Annu. Rev. Mater. Res.*, 32:163–194, 2002.

[46] F. Lemke, W. Rheinheimer, and M. J. Hoffmann. Sintering and grain growth in $SrTiO_3$: Impact of defects on kinetics. *J. Ceram. Soc. of Japan*, 124:346–353, 2016.

[47] J. E. Guyer, D. Wheeler, and J. A. Warren. FiPy: Partial differential equations with python. *Comput. Sci. Eng.*, 11:615, 2009.

[48] D. Freedman and P. Diaconis. On the histogram as a density estimator: L2 theory. *Probability Theory and Related Fields*, 57:453–476, 1981.

[49] M. Bäurer, H. Kungl, and M. J. Hoffmann. Influence of Sr/Ti stoichiometry on the densification behavior of strontium titanate. *J. Am. Ceram. Soc.*, 92:601–606, 2009.

[50] H. Sternlicht, W. Rheinheimer, R. E. Dunin-Borkowski, M. J. Hoffmann, and W. D. Kaplan. Characterization of grain boundary disconnections in $SrTiO_3$ part I: The dislocation component of grain boundary disconnections. *J. Mater. Sci.*, 54:3694, 2019.

[51] G. Bolling and W. Winegard. Some effects of impurities on grain growth in zone-refined lead. *Acta Metall.*, 6:288–292, 1958.

[52] J. W. Rutter and K. T. Aust. Kinetics of grain boundary migration in high-purity lead containing very small additions of silver and of gold. *Trans. AIME*, 218:682, 1960.

[53] K. Barmak, E. Eggeling, D. Kinderlehrer, R. Sharp, S. Ta'asan, A. D. Rollett, and K. R. Coffey. Grain growth and the puzzle of its stagnation in thin films: The curious tale of a tail and an ear. *Progr. Mater. Sci.*, 58:987, 2013.